Published in final edited form as:
Nanotechnology. 2013 September 6; 24(35): . doi:10.1088/0957-4484/24/35/355101.

'Living' PEGylation on gold nanoparticles to optimize cancer cell uptake by controlling targeting ligand and charge densities

Hongwei Chen[1,*,#], **Hayley Paholak**[1,#], **Masayuki Ito**[2], **Kanokwan Sansanaphongpricha**[1], **Wei Qian**[2], **Yong Che**[2], and **Duxin Sun**[1,*]

[1]Department of Pharmaceutical Sciences, College of Pharmacy, University of Michigan, Ann Arbor, Michigan 48109, USA

[2]IMRA America, Inc. 1044 Woodridge Avenue, Ann Arbor, Michigan 48105, USA

Abstract

We report and demonstrate biomedical applications of a new technique – 'living' PEGylation – that allows control of the density and composition of heterobifunctional PEG (HS-PEG-R) on gold nanoparticles (AuNPs). We first establish 'living' PEGylation by incubating HS-PEG_{5000}-COOH with AuNPs (~20 nm) at increasing molar ratios from zero to 2000. This causes the hydrodynamic layer thickness to differentially increase up to 26 nm. The controlled, gradual increase in PEG-COOH density is revealed after centrifugation, based on the ability to re-suspend the pellet and increase the AuNP absorption. Using a fluorescamine-based assay we quantify differential HS-PEG_{5000}-NH_2 binding to AuNPs, revealing it is highly efficient until AuNP saturation. Furthermore, the zeta potential incrementally changes from −44.9 to +52.2 mV and becomes constant upon saturation. Using 'living' PEGylation we prepare AuNPs with different ratios of HS-PEG-RGD and incubate them with U-87 MG and non-target cells, demonstrating that targeting ligand density is critical to maximizing the targeting efficiency of AuNPs to cancer cells. We also sequentially control the HS-PEG-R density to develop multifunctional nanoparticles, conjugating positively-charged HS-PEG-NH_2 at increasing ratios to AuNPs containing negatively-charged HS-PEG-COOH to reduce uptake by macrophage cells. This ability to minimize non-specific binding/uptake by healthy cells could further improve targeted nanoparticle efficacy.

Keywords

Gold nanoparticles; PEGylation; Cancer cell targeting; Ligand density; Non-Specific uptake

1. Introduction

The ability to target delivery of nanoparticles to solid tumors and minimize their distribution to non-target sites are critical tasks in the development of cancer nanomedicine for *in vivo* molecular imaging and targeted therapy [1]. It is generally accepted that the presentation of

Correspondence should be addressed to: Duxin Sun, PhD, or Hongwei Chen, PhD, Department of Pharmaceutical Sciences, College of Pharmacy, The University of Michigan, 428 Church Street, Ann Arbor, MI 48109, duxins@umich.edu (D. Sun); or hongweic@umich.edu (H. Chen).
[#]Hongwei Chen and Hayley Paholak contributed equally to this paper.

Supporting Information Available: Additional figures of PEGylation with HS-PEG-OCH_3, PEGylation using chemically made AuNPs, TEM images of AuNPs after PEGylation, synthesis of HS-PEG-RGD, PEGylation of using HS-PEG-RGD, and a photograph of both laser- and chemically-made gold colloids after PEGylation using excessive HS-PEG-R or by partially PEGylating the AuNPs with different HS-PEG-R sequentially. This material is available free of charge via the internet.

The authors declare no competing financial interest.

multiple targeting ligands on nanoparticle surfaces can improve cell targeting. A variety of tumor-targeting ligands, such as the RGD peptide [2], epidermal growth factor (EGF) [3], folate [4], transferrin (Tf) [5], or antibodies and antibody fragments, such as a single-chain variable fragment (scFv) [6], have been used to facilitate the binding/uptake of carriers to target cells. However, little work has been done to determine whether an optimal ligand density exists [7]. In order to achieve an effective level of nanoparticles in the targeted tissue or tumor site, targeted nanoparticles should transition from circulating blood to the tissue of interest and bind to their molecular target as a first step in nanoparticle retention or cellular internalization. The reality is that even with targeting ligands, many types of systemically delivered nanoparticles are rapidly cleared from the blood stream through non-specific uptake by the reticuloendothelial system (RES) and the mononuclear phagocytic system (MPS) in the liver, spleen, and bone marrow [8]. This results in reduced bioavailability of the targeting agents, a low therapeutic index, and potential toxicity to normal organs. Therefore, enhancing target-ligand interactions and reducing both non-specific binding by biomolecules and uptake of nanoparticles by the RES are major challenges for improving the sensitivity and specificity of biomarker targeted nanoparticles.

Gold nanoparticles (AuNPs) have been attracting increasingly widespread interest as a multifunctional platform for various applications in biology and medicine [9–12]. AuNPs are particularly useful for these applications, as they can function as contrast agents in optical imaging [13–15], sensitizers for Raman scattering-based diagnostic probes [16–18], and as vectors for photothermal therapy [19–21]. A key feature of nanoparticle agents is their multifunctionality; the ability to append ligands, antibodies, imaging labels, drugs, or other molecules to nanoparticles enables targeted molecular imaging and therapy [22–24]. AuNPs serve as an excellent platform to attach functional moieties facilely due to a strong Au-S linkage formed using thiol-terminated poly(ethylene glycol) (HS-PEG-R) molecules [25].

For biomedical applications of AuNPs using PEG molecules with functional R-groups, the ability to control the PEG-R chain density can have profound implications. An optimal targeting ligand density on nanoparticles might enhance their targeting efficiency to tumors with minimized non-specific uptake by healthy tissues and organs. While advances have been made in the development of functionalized AuNPs, current AuNP synthesis approaches lack the ability to subsequently control PEG chain density and therefore the density and stability of the functional groups coating the AuNPs [26–30]. Traditional PEGylation on chemically made AuNPs is typically achieved through a ligand exchange process by using thiol-terminated PEG molecules to replace the original capping ligands (e.g., citrate). Therefore, stabilization of AuNPs during PEGylation requires excessive PEG molecules [16, 26, 27], making it impossible to control the PEG-R chain density on AuNPs.

Here we report a ‘living’ PEGylation technique with the ability to control the density of functional PEG chains, and thus the targeting ligand or charge density, on AuNPs. The principle behind this technique is similar to that of living polymerization, which is widely used by polymer chemists to control chain length by changing the ratio of monomer/initiator to build di-block or tri-block copolymers [31]. For our studies we used AuNPs made by femtosecond laser ablation [32, 33]. Different from traditional AuNPs made by chemical synthesis, AuNPs made by femtosecond laser ablation have ‘naked’ surfaces without any capping ligands. Consequently, it is possible to develop stable AuNP formulations while controlling the molar ratio of HS-PEG-R/AuNP, when it is below the saturation ratio. PEGylation is so efficient that essentially all of the added HS-PEG-R molecules become bound to the AuNPs. Using ‘living’ PEGylation, we investigate the potential to improve key requirements for targeted nanomedicine. First we control the targeting ligand density on AuNPs to optimize the specific targeting ability to cancer cells. Furthermore, via ‘living’

PEGylation we can add PEG-R chains in sequential steps to AuNPs, controlling the density of different functional PEG-R chains on the nanoparticles. Using this controlled, sequential PEGylation we develop double-charged AuNPs, conjugating positively-charged HS-PEG-NH_2 at increasing ratios to AuNPs containing negatively-charged HS-PEG-COOH, to reduce uptake by macrophage cells. Therefore, this unique PEGylation process using laser-produced AuNPs facilitates unprecedented control over the development of multifunctional nanoparticles, with implications for both therapeutic and diagnostic nanoparticle applications.

2. Experimental section

Materials and Instrumentation

HS-PEG_{5000}-NH_2, HS-PEG_{5000}-COOH, and ortho-pyridyl-disulfide-PEG-succinimidyl ester (OPSS-PEG-NHS, 5 kD) were purchased from Creative PEGWorks (Winston-Salem, NC). HS-PEG_{5000}-OCH_3 was purchased from NanoCS. Cyclo (Arg-Gly-Asp-*D*-Phe-Lys) (RGD-NH_2, Peptides International, Inc) were used as received. Fluorescamine, Ellman's reagents, and all other solvents were obtained from Sigma-Aldrich. Milli-Q water (18.2 MΩ cm) was prepared using Milli-Q Academic water purification system (Billerica, MA). UV visible spectra were recorded in a BioTek micro plate reader (Synergy 2). A luminescence spectrometer LS-50B (Perkin Elmer, UK) was used to characterize the emission spectra of the fluorescamine assay. The nanoparticle hydrodynamic size and zeta potential were measured using a dynamic light scattering (DLS) instrument (Malvern Zeta Sizer Nano S-90) equipped with a 22 mW He-Ne laser operating at $\lambda = 632.8$ nm. The AuNPs were viewed by transmission electron microscopy (TEM) (Philips CM-100 60 kV).

Preparation of AuNPs

AuNPs were generated by laser ablation with the following laser parameters. Femtosecond pulses delivered from the above-stated laser system (repetition rate of 100 kHz, 10 μJ pulse energy, 700 fs pulse width centered at a wavelength of 1.045 μm) were focused onto a spot size of about 50 μm on a gold metal plate (99.99% purity) placed on the bottom of a glass vessel filled with 20 mL of deionized water. After a couple of days of aging, the top clear red solution was collected.

PEGylation of AuNPs with HS-PEG-R

In a typical process, 1.0 mL of AuNP solution (1.0 nM) was added with 10 μL of HS-PEG-R solution at different concentrations to obtain the following final molar ratios: 0, 50, 80,100, 150, 200, 300, 400, 500, 600, 800, 1000, 2000. The reaction mixture was vortexed immediately and then incubated at room temperature for two days. After PEGylation, half of each solution was used for measuring absorption spectra, hydrodynamic size and zeta potential. The other half of each solution was centrifuged at 14000 rpm for 20 min and re-dispersed with Milli-Q water by gentle shaking. This process was repeated three times. For PEGylation using HS-PEG-NH_2, the supernatant after the first centrifugation was carefully collected and also centrifuged two more times to remove any remaining AuNPs. The resultant supernatant solution was analyzed via the fluorescamine assay. For the sequential PEGylation with a combination of both HS-PEG-COOH and HS-PEG-NH_2, AuNPs were first partially PEGylated with HS-PEG-COOH, then different amounts of HS-PEG-NH_2 was added.

Quantification of Unbound HS-PEG-NH_2 in Supernatant

For a typical fluorescamine assay, 400 μL of each supernatant solution or calibration solution (without mixing with AuNPs) was mixed with 20 μL of Na_2HPO_4 (0.2 M, pH 10.0) and then 4.0 μL of fluorescamine solution in DMSO (2 mM). After 15 min, fluorescence

spectra (λ_{ex}: 390 nm, λ_{em}: 480 nm) were recorded. The fluorescence intensities at 480 nm for each solution were plotted as a function of the HS-PEG-NH_2/AuNP molar ratio.

Preparation of HS-PEG-RGD and PEGylation to AuNPs

To a 25-mL round bottom flask, 50.1 mg of OPSS-PEG-NHS were dissolved in 1.0 mL of benzene. The solution was frozen before evaporating the solvent under reduced pressure to remove trace amounts of water. Anhydrous DMF (10 mL) was added to dissolve the powder, then 6.1 mg of c(RGDfK) was added and mixed together, and finally *N, N*-Diisopropylethylamine was added. The solution was stirred at room temperature for 48 h. Dithiothreitol (DTT) was then added to the reaction mixture and stirred for additional 2 h to reduce the disulfide and obtain a free thiol at the end of the PEG-RGD polymer. The resultant powder was harvested through precipitation in dry diethyl ether. Unconjugated RGD was removed by a size exclusion NAP-5 Column (GE Healthcare, UK) and the purified HS-PEG-RGD was confirmed by HPLC. PEGylation using HS-PEG-RGD to AuNPs at different molar ratios is carried out the same as for HS-PEG-COOH. After centrifugation twice, the final AuNP pellets were re-suspended in 0.5 mL Milli-Q H_2O to concentration the solution 20 times.

Cell Culture and Preparation

The U-87 MG brain cancer (glioblastoma), MCF-7 breast cancer, and RAW 264.7 macrophage cell lines were maintained as adherent cultures and grown as monolayers in a humidified incubator (95% air; 5% CO_2) at 37 °C in a Petri dish containing medium supplemented with antibiotic-antimycotic and 10% heat-inactivated fetal bovine serum (FBS). To test targeting efficiency of AuNPs with different PEG-RGD density, cells were seeded into 6-well plates and left overnight. Cell numbers (3.0×10^5 U-87 MG/well, 7.3×10^5 MCF-7/well, 2.7×10^5 RAW 264.7/well) were counted using a Countess automated cell counter (Invitrogen, USA). After exposure to AuNPs (5 nM) formulated with different ratios of PEG-RGD in complete media supplied with 10% FBS at 37 °C for 4 h (U-87 MG, MCF-7) or 8 h (RAW 264.7), cells were washed with PBS twice and digested in aqua regia for 2 h. The aqua regia solutions were transferred to 15 mL centrifuge tubes and the final volumes were adjusted using Milli-Q water. The final gold content was measured using inductively coupled plasma optical emission spectrometry (ICP-OES). To test non-specific uptake of double-charged AuNPs with HS-PEG-COOH and HS-PEG-NH_2, macrophage cells (2.7×10^5/well) were seeded into 6-well plates overnight and then incubated with 1.0 nM double-charged AuNPs in complete media at 37 °C for 4 h. AuNPs coated with a single type of thiolated PEG (HS-PEG-OCH_3, HS-PEG-COOH, or HS-PEG-NH_2) were used as controls.

3. Results and discussion

We first mixed AuNPs (~20 nm in diameter based on TEM imaging) with HS-PEG-COOH at different HS-PEG-COOH/AuNP molar ratios from zero to 2000. This molar ratio range was chosen based on the surface area of 20 nm AuNP and the footprint of PEG molecules. For PEGylation we selected thiolated PEG_{5000}, which is most widely used to modify gold nanoparticles [30, 34]. The thiol concentration (>95%) was confirmed by an Ellman's test. During PEGylation the AuNP concentration was fixed at 1.0 nM, determined by correlating our measured extinction spectra to the experimentally determined extinction cross-section data (8.8×10^8 $M^{-1}cm^{-1}$ for AuNPs with a diameter of 20 nm) [35].

Control over the AuNP PEGylation process was monitored by the change in particle size. As shown in Figure 1, the change in hydrodynamic layer thickness differentially increased with increasing molar ratios of HS-PEG-COOH/AuNP and reached a constant at 26 nm after the

AuNP surface was saturated at molar ratio of 500. This revealed an increase in PEG chain density on AuNP surfaces upon increasing the HS-PEG-COOH/AuNP molar ratio. For free PEG molecules in a good solvent, the radius of gyration R_g can be empirically calculated as shown in equation (1):

$$R_g[nm]=0.181 \times N^{0.58} \quad (1)$$

where N is the number of ethylene glycol (EG) monomer units per PEG chain [36]. For the PEG_{5000} used here, R_g is 2.8 nm and the size increase should be around 11.2 nm (2.8 × 4) if the PEG chains form isolated hemispheres (mushroom) on the surface with a critical PEG density σ^* ($1/\pi R_g^2$) around 0.04 PEG/nm^2. At a molar ratio of 500 the PEG density σ is around 0.4 PEG/nm^2, which is 10 times higher than the critical grafting density [29]. The grafting PEG chains are most likely reconfigured, stretching out in a brush conformation as shown in the insert of Figure 1. This explains why the hydrodynamic layer thickness (ΔD) is more than four times the radius of gyration.

Figure S1(a) shows the optical spectra of AuNPs at all HS-PEG-COOH/AuNP ratios. The overlapping curves and the constant OD reveal that there is no loss of AuNPs after PEGylation for each of the HS-PEG-COOH/AuNP molar ratios. This is in contrast to traditional PEGylation to citrate-capped AuNPs made by chemical synthesis, which requires a large excess of thiolated PEG molecules [27]. Otherwise, the citrate-capped gold colloids will not be stable [26]. The high colloidal stability of laser-made AuNPs after PEGylation with different molar ratios is attributed to the highly negatively-charged ‘naked’ surface in Figure S1(b), which shows that the zeta potential is independent of the HS-PEG-COOH/AuNP molar ratio. Although there are not any capping ligands on the AuNP surfaces before PEGylation, the AuNPs made by femtosecond pulse laser ablation have a natural negative surface with a zeta potential of about −33.3 mV. The negatively-charged surface is caused by partial oxidation from the oxygen present in solution, followed by proton transfer to adjacent hydroxide ions [37]. This natural negative surface free of capping ligands makes these laser-generated gold colloids unique from traditional ones in that PEGylation can be controlled.

The differential PEG-COOH chain densities on AuNPs after PEGylation at varying molar ratios of HS-PEG-COOH/AuNP were confirmed by centrifuging the solutions and re-suspending the pellet of AuNPs. Figure 2 compares the optical densities (OD) of the absorption peaks after centrifugation for each HS-PEG-COOH/AuNP molar ratio, and Figure S2 shows typical absorption spectra. The data in Figure 2 clearly demonstrate the controlled increase in HS-PEG-COOH density with each AuNP formulation, as the HS-PEG-COOH/AuNP molar ratio dictates the stability of the formulations after centrifugation. For ratios less than 100 the AuNP pellet could not be re-dispersed after centrifugation, revealing the PEG-COOH chain density is too low to maintain a stable formulation. As the molar ratio increased from 100 to 300 the OD number increased by 25 times, with a relative change from 4% to 100% when compared to the OD before centrifugation, respectively. The data also indicate that even though the AuNP surface is not fully covered with PEG at a molar ratio of 300, the AuNPs are stable against centrifugation. This differential stability based on the changing HS-PEG-COOH density on AuNPs is also apparent in Figure S2. As the molar ratio increased from 100 to 200 more AuNPs were recovered after centrifugation, determined by the increase of the absorption peak at 524 nm. However, detection of a second, smaller peak (or ‘bump’) at ~650 nm suggests these partially PEGylated AuNPs tend to form aggregates after centrifugation, indicating a higher PEG-COOH chain density is required to maintain stability.

To further analyze the PEGylation efficiency of our laser-made AuNPs we incubated HS-PEG-NH_2 with AuNPs at increasing molar ratios, which allowed us to use a fluorescamine-based assay to quantify HS-PEG-NH_2 binding to AuNPs [27]. We varied the HS-PEG-NH_2 concentration during incubation from 50 to 2000 nM while keeping the AuNP concentration constant at 1.0 nM. First we monitored the zeta potential values of the PEGylated AuNPs as shown in Figure 3(a). They gradually transformed from highly negative (−44.9 mV) at low molar ratios to highly positive (reaching +52.2 mV) and remained constant for molar ratios higher than 500, revealing the increasing PEG-NH_2 chain density on the AuNPs until the surfaces become saturated. Successful differential PEGylation was further demonstrated by monitoring the size increase after PEGylation with increasing HS-PEG-NH_2/AuNP molar ratios, as shown in Figure S3. The data show that the hydrodynamic layer thickness incrementally increased up to 26 nm at the saturated HS-PEG-NH_2/AuNP molar ratio of 500, which is consistent with the PEGylation using HS-PEG-COOH. The data combined clearly reveal a controlled increase in the PEG-NH_2 chain density as we increased the HS-PEG-NH_2/AuNP molar ratio.

Using the fluorescamine-based assay we established a linear calibration curve for free HS-PEG-NH_2 (Figure S4(b)) based on the peak intensity at 480 nm observed in the fluorescence spectra at PEG concentrations from 50 to 2000 nM (Figure S4(a)). In this assay a non-fluorescent fluorescamine reacts with a primary amine to generate a compound that emits fluorescence at 480 nm when excited at 390 nm, as shown in Scheme S1. Originally developed for quantification of primary amines in biomolecules, this assay has sensitivity on the pM scale [38]. After incubation with AuNPs followed by centrifugation, we quantified the concentration of free HS-PEG-NH_2 in the supernatants as shown in Figure 3(b) (corresponding fluorescence spectra shown in Figure S4(c)). Although the HS-PEG-NH_2 concentration increased 10 times up to 500 nM there was no obvious fluorescence increase after measuring the supernatants, whereas for ratios higher than 500 the supernatant fluorescence began to increase. This revealed that the gradual increase in HS-PEG-NH_2 binding to AuNPs is highly efficient below saturation at 500 nM, and this point of saturation is consistent with our zeta potential and size change measurements. Measuring the PEG concentration in supernatants to estimate the PEG chain density on AuNPs is a widely used method [27, 30]. However, in previous reports using chemically prepared AuNPs, more than 90% of the added HS-PEG-R molecules remained in the supernatants because of the excessive HS-PEG-R required to stabilize AuNPs during PEGylation [26]. In our case as most of the added HS-PEG-NH_2 molecules were bound to AuNPs, our assay measurements are more sensitive than those in the previous reports. The combined experiments using HS-PEG-COOH and HS-PEG-NH_2 demonstrate a highly efficient PEGylation process that allows control of the PEG density on AuNPs by manipulating the molar ratio of HS-PEG-R/AuNP, while the ratio is less than the saturated one. This technique is similar to living polymerization, through which a polymer chain length can be controlled by the ratio of monomer/initiator. Thus we termed this technique ‘living’ PEGylation.

One important application of ‘living’ PEGylation is to control the targeting ligand density on AuNPs to improve specific targeting efficiency. Consequently, we synthesized HS-PEG-RGD to investigate specific targeting efficacy of AuNPs to $\alpha_v\beta_3$ integrin receptors. The targeting peptide conjugation to PEG was performed based on traditional coupling reactions between NHS ester and amine groups using thiol-protected OPSS-PEG-NHS and cyclo(RGDfk)-NH_2 followed by deprotection of the thiol groups using DTT (Scheme S2) [39, 40]. The expected HS-PEG-RGD was purified by a size exclusion column and confirmed by HPLC, with the retention time shifting from 16.87 to 19.64 min compared to unconjugated RGD (Figure S5) [42]. The characteristic peak of the optical spectrum of purified HS-PEG-RGD is identical to RGD alone, revealing the successful peptide conjugation (Figure S6). An Ellman’s test also confirmed effective deprotection to reveal a

terminal free thiol. PEGylation using HS-PEG-RGD on AuNPs with serial HS-PEG-RGD/AuNP molar ratios was done as described for HS-PEG-COOH. Hydrodynamic size and zeta potential measurements were used to monitor the PEGylation process (Figure S7). As expected, the hydrodynamic size of PEGylated AuNPs incrementally increased as we increased the molar ratio of HS-PEG-RGD/AuNP below the saturation ratio (Figure S7(a)). The zeta potential data revealed that all PEG-RGD-modified AuNPs have highly negatively charged surfaces (~−40 mV) (Figure S7(b)). Taken together, the data clearly show that AuNPs with different PEG-RGD densities on the surface were successfully obtained in a controlled way.

Specific cellular targeting efficiency to cancer cells was tested using two cancer cell lines: U-87 MG, positive for $\alpha_v\beta_3$ integrin receptors, and MCF-7, classified negative for the receptor and serving as an example of non-target cells. The gold content inside the cells after digestion with aqua regia was measured by ICP-OES. Using the same conditions as for live cell incubations the stability of these PEGylated AuNPs in media was first confirmed by the optical spectra in Figure S8, as there is no change of peak OD over four hours in DMEM plus 10% FBS.

The effect of the PEG-RGD/AuNP ratio on cellular uptake after incubation with AuNPs is shown in Figure 4(a) for U-87 MG cells and in Figure 4(b) for MCF-7 cells. These data clearly show that U-87 MG cells uptake more AuNPs modified with RGD than MCF-7 cells, which demonstrates the specific targeting ability of the RGD peptide [41, 42]. Furthermore, for incubations with AuNPs with PEG-RGD/AuNP molar ratios of 50 or lower U-87 MG cells demonstrate consistently increased uptake as the PEG-RGD/AuNP molar ratio is increased, with uptake reaching up to 3.7 pg/cell as the ratio increased to 50. On the contrary, MCF-7 cells uptake is independent of PEG-RGD density change in this range, which is around 0.2 pg/cell and 18-fold lower than in U-87 MG cells. For AuNPs with PEG-RGD/AuNP molar ratios higher than 50, uptake in both U-87 MG cells and MCF-7 cells began to increase with increasing RGD density. Comparing Figures 4(a) and 4(b), the relative uptake of U-87 MG (compared to MCF-7) versus PEG-RGD chain density revealed a clear optimal targeting ligand density around 50 PEG-RGD on each AuNP that maximizes specific uptake by target cells while minimizing uptake in non-target cells.

We next incubated MCF-7 cells with AuNPs containing a control RAD peptide that does not specifically target $\alpha_v\beta_3$ integrin receptors in order to determine whether the increased gold content in MCF-7 cells for PEG-RGD/AuNP molar ratios higher than 50 was caused by non-specific uptake [43]. We found that the gold content in MCF-7 cells does not increase for even the highest PEG-RAD/AuNP molar ratios (Figure S9). This suggests that the rise in uptake observed for higher molar ratios of PEG-RGD/AuNP in Figure 4(b) is from specific uptake due to very low expression of $\alpha_v\beta_3$ integrin receptors on MCF-7 cells, triggered by a threshold RGD density. Consequently, we decided to next investigate the potential for targeting ligand density to affect non-specific uptake by macrophage cells.

Figure 5 shows the uptake of AuNPs with different PEG-RGD surface densities after incubation with macrophage cells. Similar to the trend observed in MCF-7 cells in Figure 4(b), for molar ratios below 50 the uptake is independent of the targeting ligand density while above 50 the uptake consistently increases with increasing ligand density. This suggests $\alpha_v\beta_3$ integrin receptors are present on macrophage cells [44], and this can trigger increased nanoparticle uptake at higher PEG-RGD densities on AuNPs. Taken with the results of Figure 4, this confirms it is possible to control the targeting ligand density on AuNPs and that it plays a critical role in optimizing specific targeting efficacy.

Another application of 'living' PEGylation is to control PEG-R chain densities on AuNPs in a sequential way for multifunctional purposes, like building di-block or tri-block copolymers using living polymerization. Here we investigated a two-step PEGylation process, first partially PEGylating with HS-PEG-R_1 and then PEGylating with HS-PEG-R_2 as shown in Scheme 1. As long as the AuNPs are not saturated (i.e. the molar ratio of HS-PEG-R/AuNP is lower than 500), one can control the density of functional moieties (R groups) covalently attached to AuNPs. In this sequential way, double-charged AuNPs with varying PEG-NH_2/PEG-COOH molar ratios were prepared by partially PEGylating with HS-PEG-COOH first, then adding different amounts of HS-PEG-NH_2, and finally adding more HS-PEG-COOH to saturate the surface.

The different double-charged AuNP formulations containing both HS-PEG-NH_2 and HS-PEG-COOH were incubated with RAW 264.7 macrophage cells and the uptake results are shown in Figure 6. The data show that by increasing the ratio of PEG-NH_2 on AuNPs from 50 to 300 through living PEGylation, the non-specific uptake of Au/cell (pg) gradually halved from 0.63 ± 0.01 to 0.33 ± 0.01. The reduced cell uptake can be explained by the overall surface charge becoming more neutral with controlled addition of more PEG-NH_2, as shown in Figure S10. These results are consistent with those obtained by Liu et al for AuNPs modified via zwitterionic self-assembled monolayers (SAMs) composed of both negatively- and positively-charged, thiol-containing carbon chains [45]. Compared to AuNPs modified with only negatively-charged carbon chains, as they increased the ratio of positive to negative carbon chains on the AuNP surfaces the negative zeta potential gradually increased and reduced the AuNP uptake by macrophage cells.

In Figure 6 we also observe that our double-charged AuNP formulations have less non-specific uptake than all of the control AuNPs decorated with a single type of PEG-R (i.e. -OCH_3, -COOH, -NH_2). For instance, the double-charged AuNP formulations show a relative uptake ranging from 40% to 76% when compared to AuNP-PEG-OCH_3, the control with the least uptake. As expected, the AuNP control containing only HS-PEG-NH_2 exhibits the greatest non-specific uptake due to the electrostatic attraction between the positively-charged AuNPs and the negatively-charged cell membrane [46–49]. The uptake of the negatively-charged AuNP-PEG-COOH control is greater than those for each double-charged AuNPs for two reasons. First, phagocytic cells preferentially uptake anionic particles versus those that are more neutral in charge [45, 47, 50]. Second, the zwitterionic property of double-charged AuNPs confers stealth due to a layer of tightly bound water molecules on the AuNP surface. This has been shown to reduce binding of plasma proteins, and recognition and non-specific uptake by cells [45, 46, 51–53]. This also explains why the uptake of the double-charged AuNPs is reduced even when compared to the neutral AuNP-PEG-OCH_3 control. Our uptake results for the double-charged AuNPs relative to the positively-charged and negatively-charged controls are consistent with those of Liu et al in RAW 264.7 macrophage cells [45]. Furthermore, they observed the same uptake trend based on AuNP charge/zeta potential in normal human umbilical vein endothelial cells (HUVEC) and human hepatocellular liver carcinoma cells (HepG2), with one slight difference. They found that in the macrophage cells the reduction in uptake of double-charged AuNPs relative to the negatively-charged AuNPs is greater than those observed in the two non-phagocytic cell lines, and they attribute this to the preferential uptake of anionic particles by phagocytic cells. Overall, our cellular uptake data with sequentially modified double-charged AuNPs exemplifies a second approach to reduce nanoparticle clearance by the immune system. Even greater potential to maximize specific uptake in target cells while minimizing non-specific uptake lies in an AuNP formulation containing both an optimal targeting ligand density and double-charged surface obtained by 'living' PEGylation, and merits further exploration. Our data suggests a facile and feasible approach would be to sequentially

PEGylate using negatively-charged HS-PEG-COOH and an optimal density of HS-PEG-R_1, where R_1 represents a positively-charged targeting ligand.

Enhanced stability to partial PEGylation in a sequential way makes laser-made, 'naked' AuNPs unique from chemically-made ones capped with citrate, as demonstrated in the photograph in Figure S11. While all commercial and laser-made AuNP formulations are stable if excessively PEGylated with HS-PEG-R (irrespective of charge), only laser-made AuNPs are stable after sequential PEGylation involving HS-PEG-NH_2. In AuNPs capped with citrate, this causes aggregation of the AuNPs and the solutions become black. Our work collectively demonstrates that this new PEGylation process with laser-made AuNPs facilitates creation of multifunctional AuNPs with a range of biomedical applications.

4. Conclusions

Using gold nanoparticles generated by femtosecond pulse laser ablation we revealed the unique ability to control the density of HS-PEG-R (-COOH, -NH_2, and -RGD) conjugated to AuNP surfaces for one or sequential rounds of conjugation, terming this process 'living' PEGylation. After PEGylation with HS-PEG-COOH at different molar ratios of HS-PEG-COOH/AuNP up to 2000, the hydrodynamic layer thickness incrementally increased with increasing molar ratio and became constant upon AuNP saturation. We then centrifuged and re-suspended the PEGylated AuNP to demonstrate the differential PEG chain density on the AuNP surface. As the PEG-COOH/AuNP molar ratio increased to the point of saturation, the OD for the absorption spectrum peak gradually increased up to 25 times and the AuNP recovery consistently increased. Next, PEGylation using HS-PEG-NH_2 was quantified by a fluorescamine-based assay. For differential HS-PEG-NH_2 ratios below the saturation ratio, essentially all the added HS-PEG-NH_2 bound to the AuNPs. Furthermore, as the molar ratio of HS-PEG-NH_2/AuNP increased the zeta potential incrementally changed from −44.9 to +52.2 mV and became constant upon AuNP saturation. Taken together, our results confirmed that the PEG-R chain density on AuNP surfaces can be precisely controlled by changing the molar ratio of HS-PEG-R/AuNP. Next we used 'living' PEGylation to investigate the dependence of specific targeting efficacy on targeting ligand density on nanoparticle surfaces, controlling the density of the model peptide RGD to AuNPs via HS-PEG-RGD. An optimal targeting ligand density around 50 PEG-RGD on each AuNP maximizes the specific targeting efficiency to U-87 MG cancer cells. Additionally, we sequentially conjugated HS-PEG-COOH and HS-PEG-NH_2 to AuNPs to create double-charged AuNPs with precise control over the PEG-NH_2/PEG-COOH ratio to reduce non-specific uptake by macrophage cells. This unique PEGylation process facilitates unprecedented control in the synthesis of multifunctional nanoparticles, with implications for both therapeutic and diagnostic nanoparticle development.

Supplementary Material

Refer to Web version on PubMed Central for supplementary material.

Acknowledgments

This work is supported by National Institutes of Health grants RO1CA120023 (D. S.) and a collaborative grant from IMRA America, Inc.

References

1. Phillips MA, Gran ML, Peppas NA. Targeted nanodelivery of drugs and diagnostics. Nano Today. 2010; 5:143. [PubMed: 20543895]

2. de la Zerda A, Bodapati S, Teed R, May SY, Tabakman SM, Liu Z, Khuri-Yakub BT, Chen XY, Dai HJ, Gambhir SS. Family of enhanced photoacoustic imaging agents for highsensitivity and multiplexing studies in living mice. ACS Nano. 2012; 6:4694. [PubMed: 22607191]
3. Mickler FM, Mockl L, Ruthardt N, Ogris M, Wagner E, Brauchle C. Tuning nanoparticle uptake: live-cell imaging reveals two distinct endocytosis mechanisms mediated by natural and artificial EGFR targeting ligand. Nano Lett. 2012; 12:3417. [PubMed: 22632479]
4. Porta F, Lamers GEM, Morrhayim J, Chatzopoulou A, Schaaf M, den Dulk H, Backendorf C, Zink JI, Kros A. Folic acid-modified mesoporous silica nanoparticles for cellular and nuclear targeted drug delivery. Adv. Healthc. Mater. 2013; 2:281. [PubMed: 23184490]
5. Yue J, Liu S, Wang R, Hu XL, Xie ZG, Huang YB, Jing XB. Transferrinconjugated micelles: enhanced accumulation and antitumor effect for transferrin-receptoroverexpressing cancer models. Mol. Pharmaceut. 2012; 9:1919.
6. Yang LL, Mao H, Wang YA, Cao ZH, Peng XH, Wang XX, Duan HW, Ni CC, Yuan QG, Adams G, Smith MQ, Wood WC, Gao XH, Nie SM. Single chain epidermal growth factor receptor antibody conjugated nanoparticles for in vivo tumor targeting and imaging. Small. 2009; 5:235. [PubMed: 19089838]
7. Elias DR, Poloukhtine A, Popik V, Tsourkas A. Effect of ligand density, receptor density, and nanoparticle size on cell targeting. Nanomed-Nanotechnol. 2013; 9:194.
8. Nie SM. Understanding and overcoming major barriers in cancer nanomedicine. Nanomedicine. 2010; 5:523. [PubMed: 20528447]
9. Giljohann DA, Seferos DS, Daniel WL, Massich MD, Patel PC, Mirkin CA. Gold nanoparticles for biology and medicine. Angew. Chem. Inter. Ed. 2010; 49:3280.
10. Doane TL, Burda C. The unique role of nanoparticles in nanomedicine: imaging, drug delivery and therapy. Chem. Soc. Rev. 2012; 41:2885. [PubMed: 22286540]
11. Dykman L, Khlebtsov N. Gold nanoparticles in biomedical applications: recent advances and perspectives. Chem. Soc. Rev. 2012; 41:2256. [PubMed: 22130549]
12. Daniel MC, Astruc D. Gold nanoparticles: Assembly, supramolecular chemistry, quantum-size-related properties, and applications toward biology, catalysis, and nanotechnology. Chem. Rev. 2004; 104:293. [PubMed: 14719978]
13. Huang X, El-Sayed IH, Qian W, El-Sayed MA. Cancer cell imaging and photothermal therapy in the near-infrared region by using gold nanorods. J. Am. Chem. Soc. 2006; 128:2115. [PubMed: 16464114]
14. Klein S, Petersen S, Taylor U, Rath D, Barcikowski S. Quantitative visualization of colloidal and intracellular gold nanoparticles by confocal microscopy. J. Biomed. Opt. 2010; 15
15. Leduc C, Jung JM, Carney RR, Stellacci F, Lounis B. Direct investigation of intracellular presence of gold nanoparticles via photothermal heterodyne imaging. ACS Nano. 2011; 5:2587. [PubMed: 21388224]
16. Qian XM, Peng XH, Ansari DO, Yin-Goen Q, Chen GZ, Shin DM, Yang L, Young AN, Wang MD, Nie SM. In vivo tumor targeting and spectroscopic detection with surface-enhanced Raman nanoparticle tags. Nat. Biotechnol. 2008; 26:83. [PubMed: 18157119]
17. Xie W, Qiu PH, Mao CB. Bio-imaging, detection and analysis by using nanostructures as SERS substrates. J. Mater. Chem. 2011; 21:5190. [PubMed: 21625344]
18. Rand D, Ortiz V, Liu YA, Derdak Z, Wands JR, Taticek M, Rose-Petruck C. Nanomaterials for X-ray imaging: gold nanoparticle enhancement of X-ray scatter imaging of hepatocellular carcinoma. Nano Lett. 2011; 11:2678. [PubMed: 21644516]
19. Hirsch LR, Stafford RJ, Bankson JA, Sershen SR, Rivera B, Price RE, Hazle JD, Halas NJ, West JL. Nanoshell-mediated near-infrared thermal therapy of tumors under magnetic resonance guidance. P. Natl. Acad. Sci. USA. 2003; 100:13549.
20. von Maltzahn G, Park JH, Lin KY, Singh N, Schwoppe C, Mesters R, Berdel WE, Ruoslahti E, Sailor MJ, Bhatia SN. Nanoparticles that communicate in vivo to amplify tumour targeting. Nat. Mater. 2011; 10:545. [PubMed: 21685903]
21. Dong WJ, Li YS, Niu DC, Ma Z, Gu JL, Chen Y, Zhao WR, Liu XH, Liu CS, Shi JL. Facile synthesis of monodisperse superparamagnetic Fe3O4 core@hybrid@Au shell nanocomposite for bimodal imaging and photothermal therapy. Adv. Mater. 2011; 23:5392. [PubMed: 21997882]

22. Park K, Lee S, Kang E, Kim K, Choi K, Kwon IC. New generation of multifunctional nanoparticles for cancer imaging and therapy. Adv Funct Mater. 2009; 19:1553–1566.
23. Minelli C, Lowe SB, Stevens MM. Engineering nanocomposite materials for cancer therapy. Small. 2010; 6:2336. [PubMed: 20878632]
24. Wang F, Wang YC, Dou S, Xiong MH, Sun TM, Wang J. Doxorubicin-tethered responsive gold nanoparticles facilitate intracellular drug delivery for overcoming multidrug resistance in cancer cells. ACS Nano. 2011; 5:3679. [PubMed: 21462992]
25. Choi CHJ, Alabi CA, Webster P, Davis ME. Mechanism of active targeting in solid tumors with transferrin-containing gold nanoparticles. P. Natl. Acad. Sci. USA. 2010; 107:1235.
26. Qian W, Murakami M, Ichikawa Y, Che Y. Highly efficient and controllable PEGylation of gold nanoparticles prepared by femtosecond laser ablation in water. J. Phys. Chem. C. 2011; 115:23293.
27. Xia XH, Yang MX, Wang YC, Zheng YQ, Li QG, Chen JY, Xia YN. Quantifying the coverage density of poly(ethylene glycol) chains on the surface of gold nanostructures. ACS Nano. 2012; 6:512. [PubMed: 22148912]
28. Nagasaki Y. Construction of a densely poly(ethylene glycol)-chain-tethered surface and its performance. Polym. J. 2011; 43:949.
29. Thierry B, Griesser HJ. Dense PEG layers for efficient immunotargeting of nanoparticles to cancer cells. J. Mater. Chem. 2012; 22:8810.
30. Walkey CD, Olsen JB, Guo HB, Emili A, Chan WCW. Nanoparticle size and surface chemistry determine serum protein adsorption and macrophage uptake. J. Am. Chem. Soc. 2012; 134:2139. [PubMed: 22191645]
31. Braunecker WA, Matyjaszewski K. Controlled/living radical polymerization: Features, developments, and perspectives. Prog. Polym. Sci. 2007; 32:93.
32. Petersen S, Barchanski A, Taylor U, Klein S, Rath D, Barcikowski S. Penetratin-conjugated gold nanoparticles - design of cell-penetrating nanomarkers by femtosecond laser ablation. J. Phys. Chem. C. 2011; 115:5152.
33. Zeng HB, Du XW, Singh SC, Kulinich SA, Yang SK, He JP, Cai WP. Nanomaterials via laser ablation/irradiation in liquid: a review. Adv. Funct. Mater. 2012; 22:1333.
34. Huang XH, Peng XH, Wang YQ, Wang YX, Shin DM, El-Sayed MA, Nie SM. A reexamination of active and passive tumor targeting by using rod-shaped gold nanocrystals and covalently conjugated peptide ligands. ACS Nano. 2010; 4:5887. [PubMed: 20863096]
35. Liu XO, Atwater M, Wang JH, Huo Q. Extinction coefficient of gold nanoparticles with different sizes and different capping ligands. Colloid Surface B. 2007; 58:3.
36. Kawaguchi S, Imai G, Suzuki J, Miyahara A, Kitano T. Aqueous solution properties of oligo- and poly(ethylene oxide) by static light scattering and intrinsic viscosity. Polymer. 1997; 38:2885.
37. Sylvestre JP, Poulin S, Kabashin AV, Sacher E, Meunier M, Luong JHT. Surface chemistry of gold nanoparticles produced by laser ablation in aqueous media. J. Phys. Chem. B. 2004; 108:16864.
38. Udenfrie.S, Stein S, Bohlen P, Dairman W. Fluorescamine - reagent for assay of amino-acids, peptides, proteins, and primary amines in picomole range. Science. 1972; 178:871. [PubMed: 5085985]
39. Gormley AJ, Malugin A, Ray A, Robinson R, Ghandehari H. Biological evaluation of RGDfK-gold nanorod conjugates for prostate cancer treatment. J. Drug Target. 2011; 19:915. [PubMed: 22082105]
40. Polyak D, Ryppa C, Eldar-Boock A, Ofek P, Many A, Licha K, Kratz F, Satchi-Fainaro R. Development of PEGylated doxorubicin-E-[c(RGDfK)(2)] conjugate for integrin-targeted cancer therapy. Polym. Advan. Technol. 2011; 22:103.
41. de la Zerda A, Bodapati S, Teed R, May SY, Tabakman SM, Liu Z, Khuri-Yakub BT, Chen X, Dai H, Gambhir SS. Family of enhanced photoacoustic imaging agents for highsensitivity and multiplexing studies in living mice. ACS Nano. 2012; 6:4694. [PubMed: 22607191]
42. Chen HW, Wang LY, Yeh J, Wu XY, Cao ZH, Wang YA, Zhang MM, Yang L, Mao H. Reducing non-specific binding and uptake of nanoparticles and improving cell targeting with an antifouling PEO-b-P gamma MPS copolymer coating. Biomaterials. 2010; 31:5397. [PubMed: 20398933]

43. Sancey L, Garanger E, Foillard S, Schoehn G, Hurbin A, Albiges-Rizo C, Boturyn D, Souchier C, Grichine A, Dumy P, Coll JL. Clustering and internalization of integrin alpha(v)beta(3) with a tetrameric RGD-synthetic peptide. Mol. Ther. 2009; 17:837. [PubMed: 19259068]
44. Byzova TV, Rabbani R, D'Souza SE, Plow EF. Role of integrin alpha(v)beta(3) in vascular biology. Thromb. Haemostasis. 1998; 80:726. [PubMed: 9843163]
45. Liu XS, Jin Q, Ji Y, Ji J. Minimizing nonspecific phagocytic uptake of biocompatible gold nanoparticles with mixed charged zwitterionic surface modification. J. Mater. Chem. 2012; 22:1916.
46. Arvizo RR, Miranda OR, Thompson MA, Pabelick CM, Bhattacharya R, Robertson JD, Rotello VM, Prakash YS, Mukherjee P. Effect of nanoparticle surface charge at the plasma membrane and beyond. Nano Lett. 2010; 10:2543. [PubMed: 20533851]
47. He CB, Hu YP, Yin LC, Tang C, Yin CH. Effects of particle size and surface charge on cellular uptake and biodistribution of polymeric nanoparticles. Biomaterials. 2010; 31:3657. [PubMed: 20138662]
48. Pillai PP, Huda S, Kowalczyk B, Grzybowski BA. Controlled pH stability and adjustable cellular uptake of mixed-charge nanoparticles. J. Am. Chem. Soc. 2013; 135:6392. [PubMed: 23527630]
49. Cho EC, Au L, Zhang Q, Xia YN. The effects of size, shape, and surface functional group of gold nanostructures on their adsorption and internalization by cells. Small. 2010; 6:517. [PubMed: 20029850]
50. Murthy AK, Stover RJ, Hardin WG, Schramm R, Nie GD, Gourisankar S, Truskett TM, Sokolov KV, Johnston KP. Charged gold nanoparticles with essentially zero serum protein adsorption in undiluted fetal bovine serum. J. Am. Chem. Soc. 2013; 135:7799. [PubMed: 23565806]
51. Holmlin RE, Chen XX, Chapman RG, Takayama S, Whitesides GM. Zwitterionic SAMs that resist nonspecific adsorption of protein from aqueous buffer. Langmuir. 2001; 17:2841.
52. Chen SF, Yu FC, Yu QM, He Y, Jiang SY. Strong resistance of a thin crystalline layer of balanced charged groups to protein adsorption. Langmuir. 2006; 22:8186. [PubMed: 16952260]
53. Zhang L, Xue H, Gao CL, Carr L, Wang JN, Chu BC, Jiang SY. Imaging and cell targeting characteristics of magnetic nanoparticles modified by a functionalizable zwitterionic polymer with adhesive 3,4-dihydroxyphenyl-L-alanine linkages. Biomaterials. 2010; 31:6582. [PubMed: 20541254]

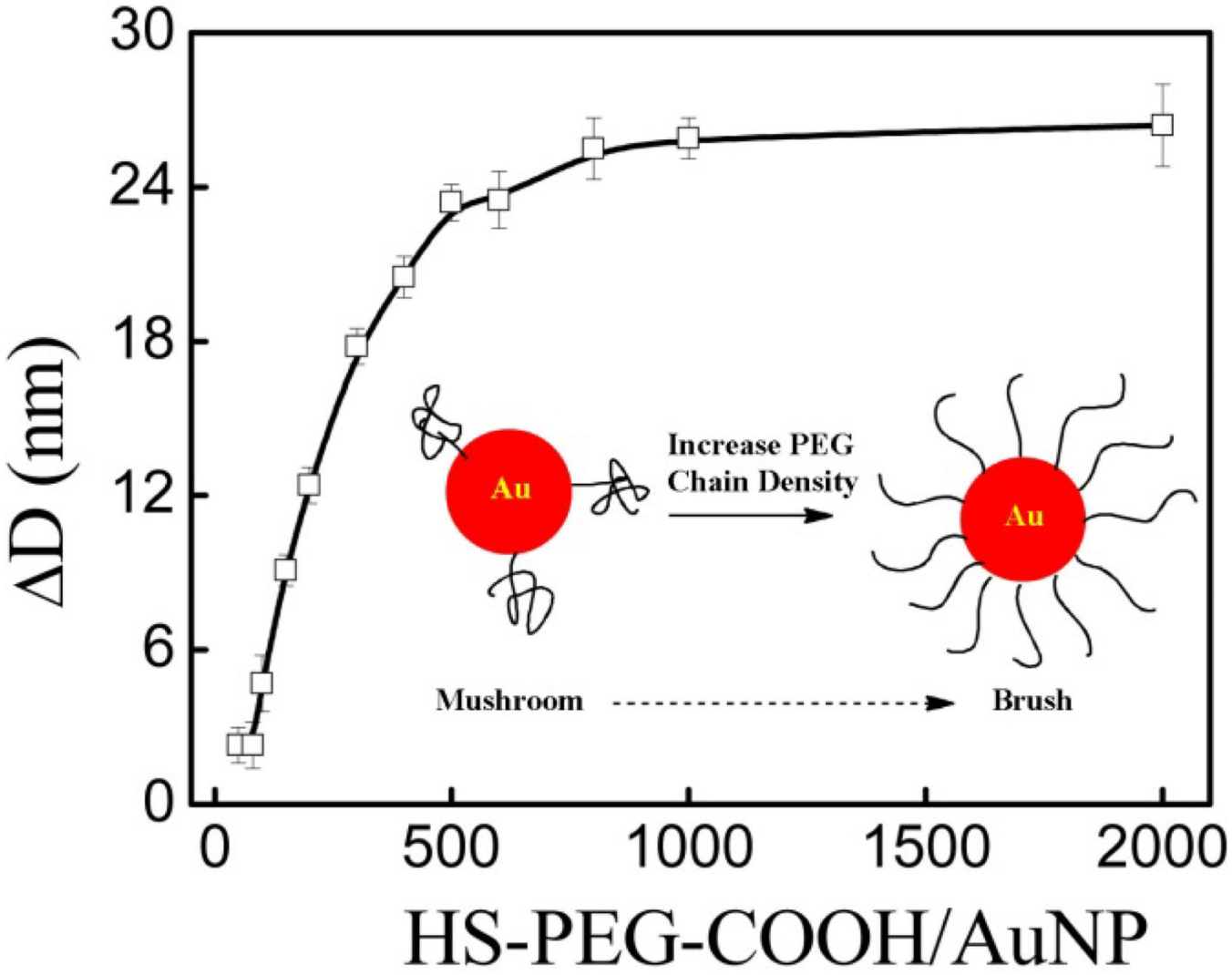

Figure 1.

Hydrodynamic size change of AuNPs PEGylated with HS-PEG-COOH at all molar ratios before centrifugation, where the insert shows a schematic illustration of the conformation change of PEGylated chains on gold nanoparticles from mushroom at lower PEG chain densities to brush at higher PEG chain densities.

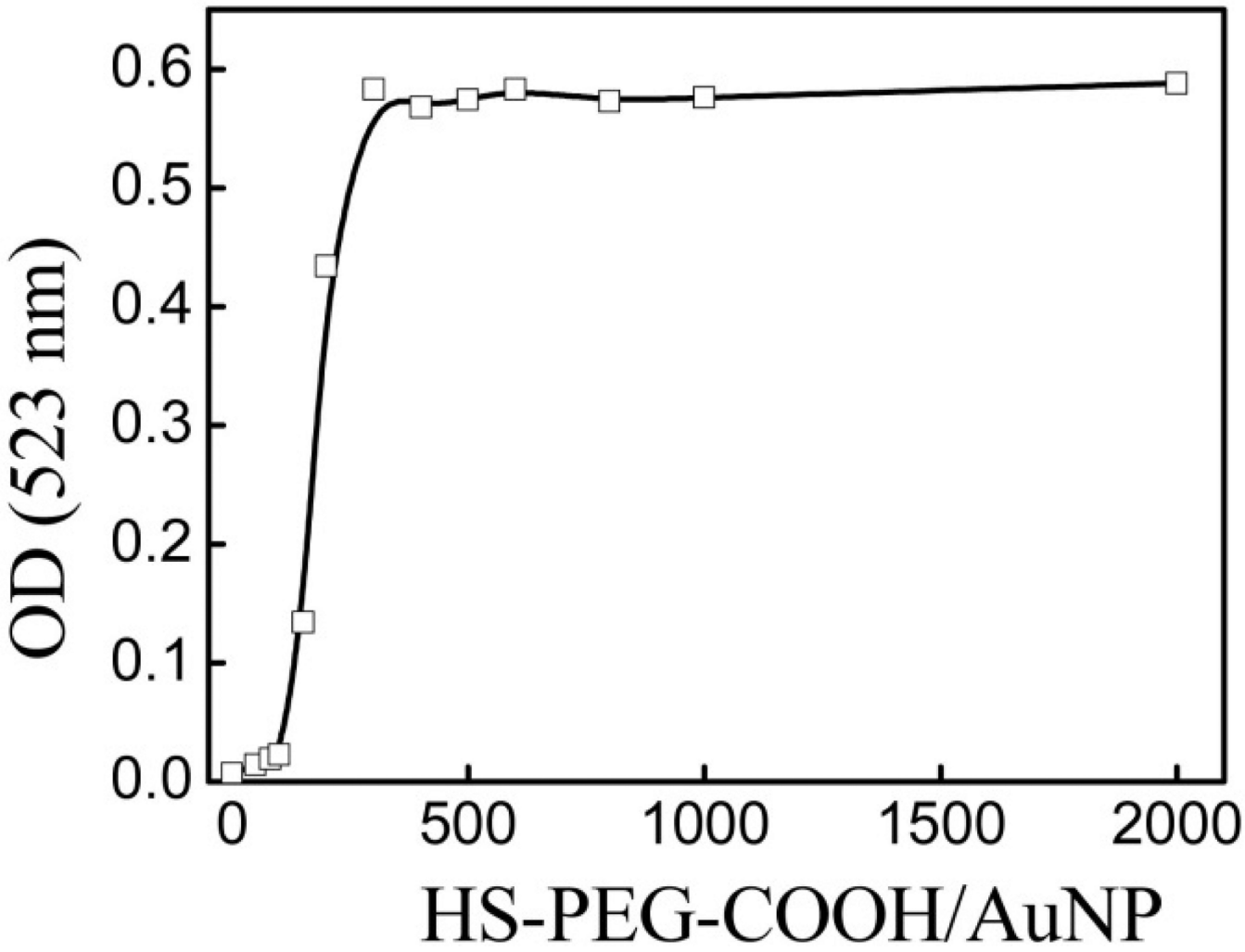

Figure 2.
Optical density at absorption peak of AuNPs PEGylated with HS-PEG-COOH at all molar ratios after centrifugation.

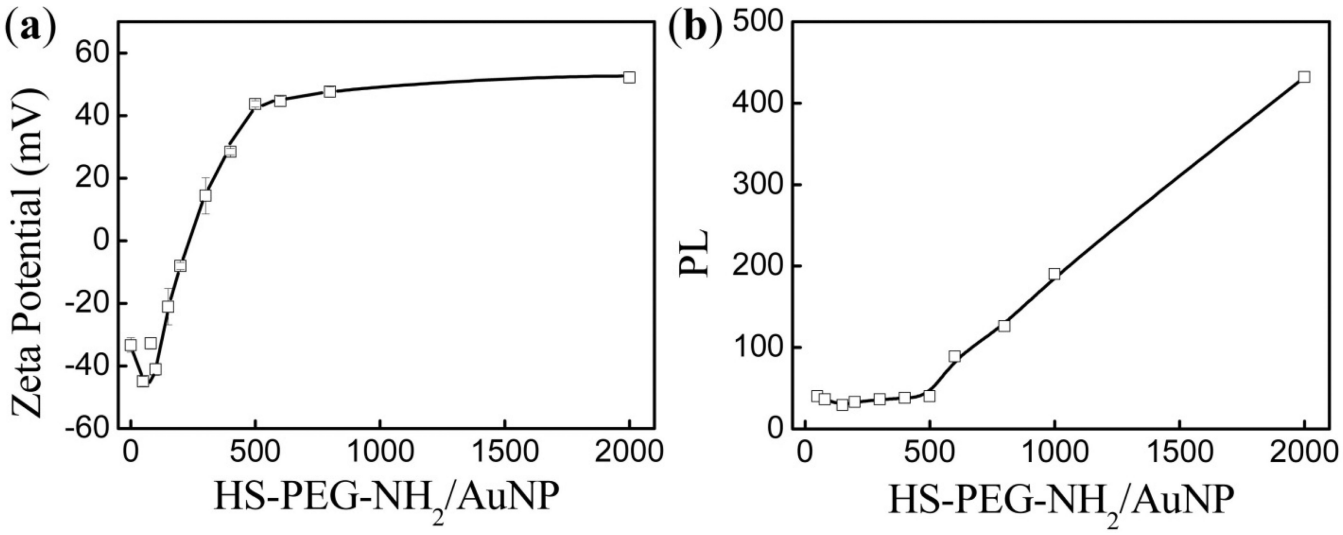

Figure 3.

(a) Zeta potential before centrifugation of AuNPs PEGylated with HS-PEG-NH_2 at all molar ratios and (b) fluorescence intensity at 480 nm, via fluorescamine-based assay, of the corresponding supernatants after centrifugation.

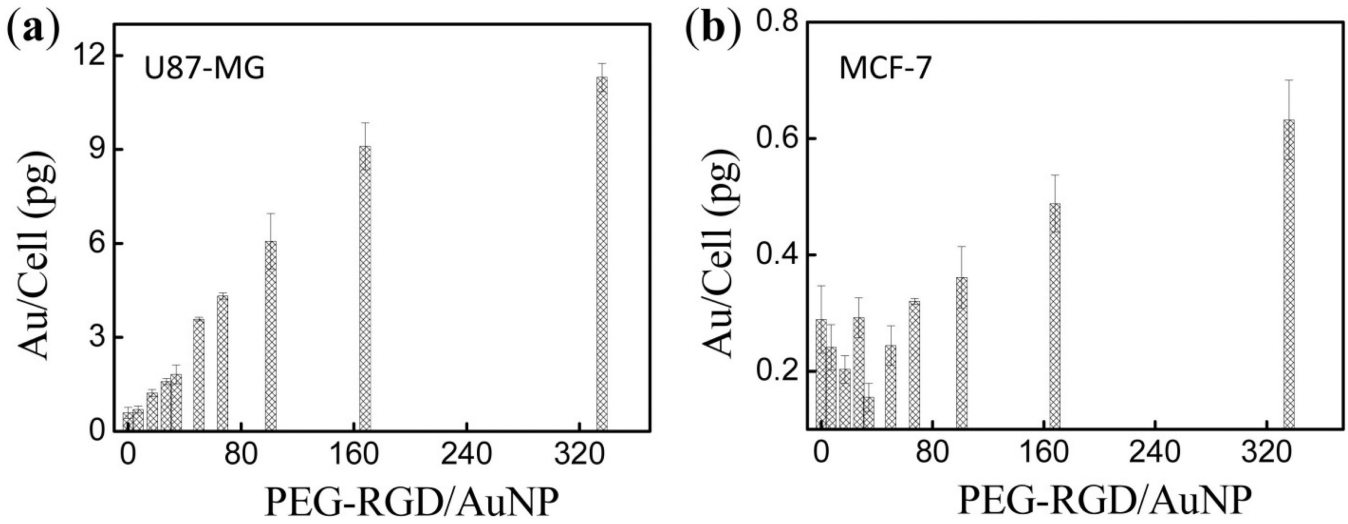

Figure 4.
Cellular uptake of AuNPs PEGylated with different PEG-RGD densities on the AuNP surface in U-87 MG (a) and MCF-7 (b) cells.

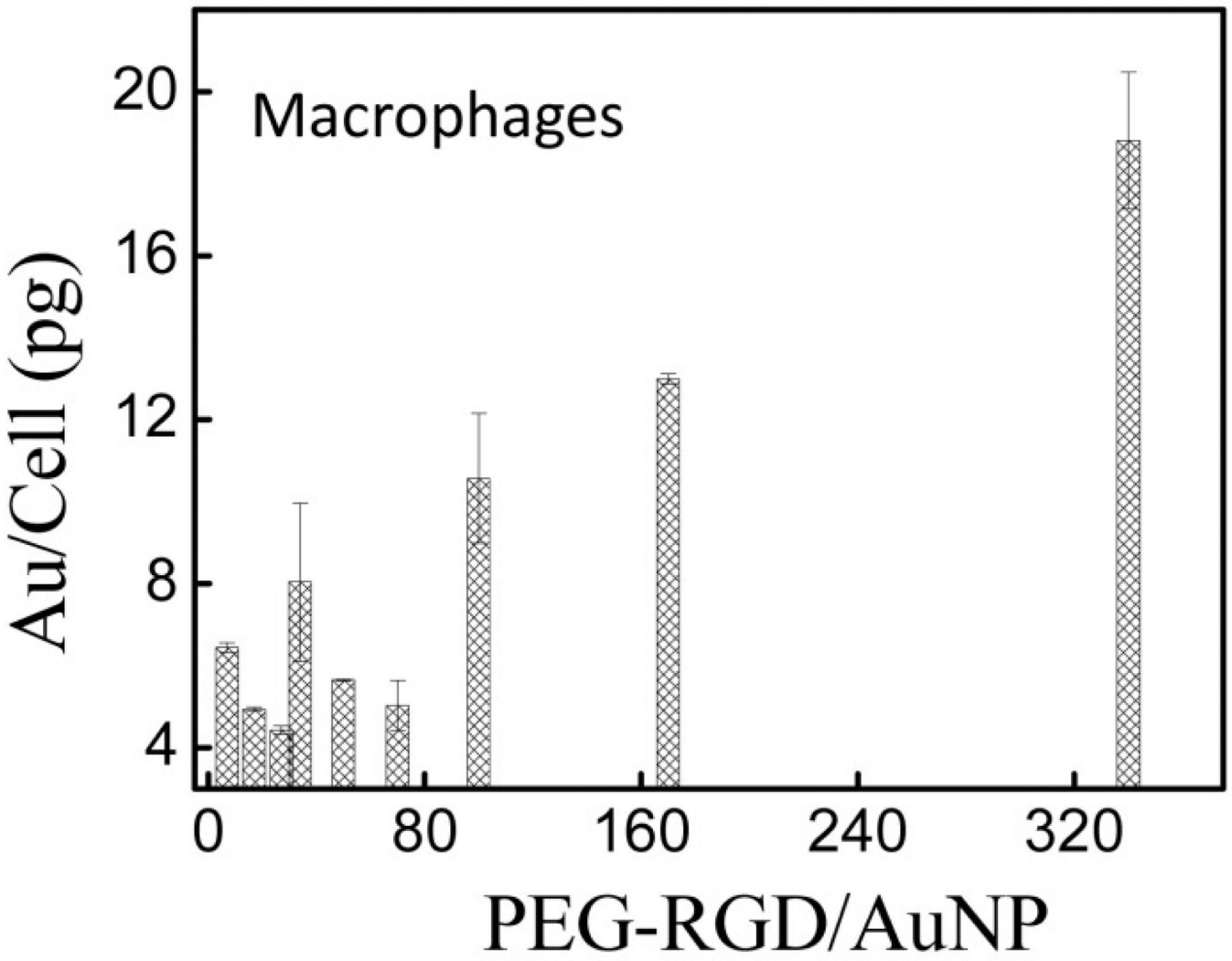

Figure 5.
Macrophage cell uptake of AuNPs PEGylated with different PEG-RGD densities on the AuNP surfaces.

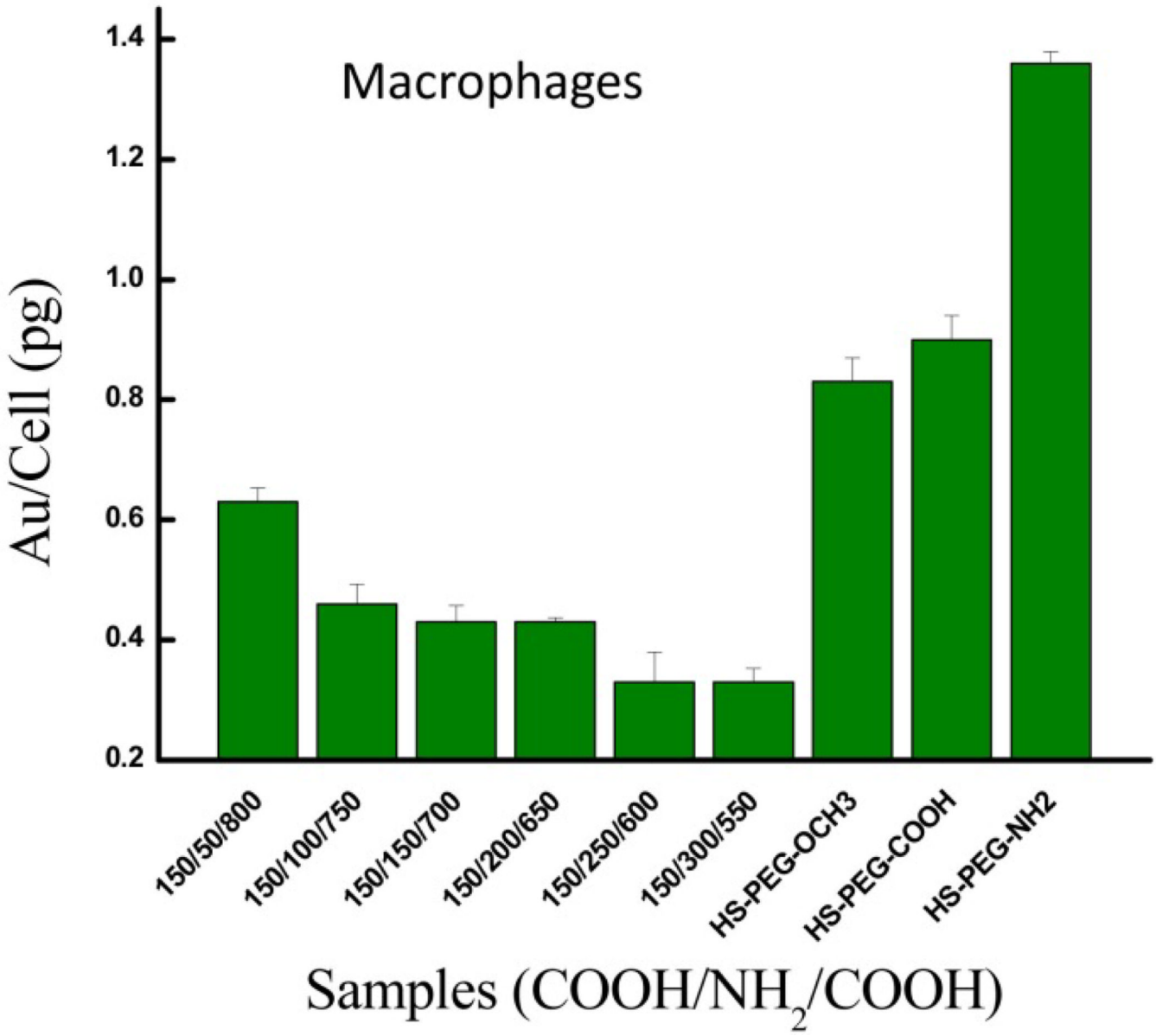

Figure 6.
Macrophage cell non-specific uptake of AuNPs decorated with PEG-R in single (control) or successive (double-charged) conjugations.

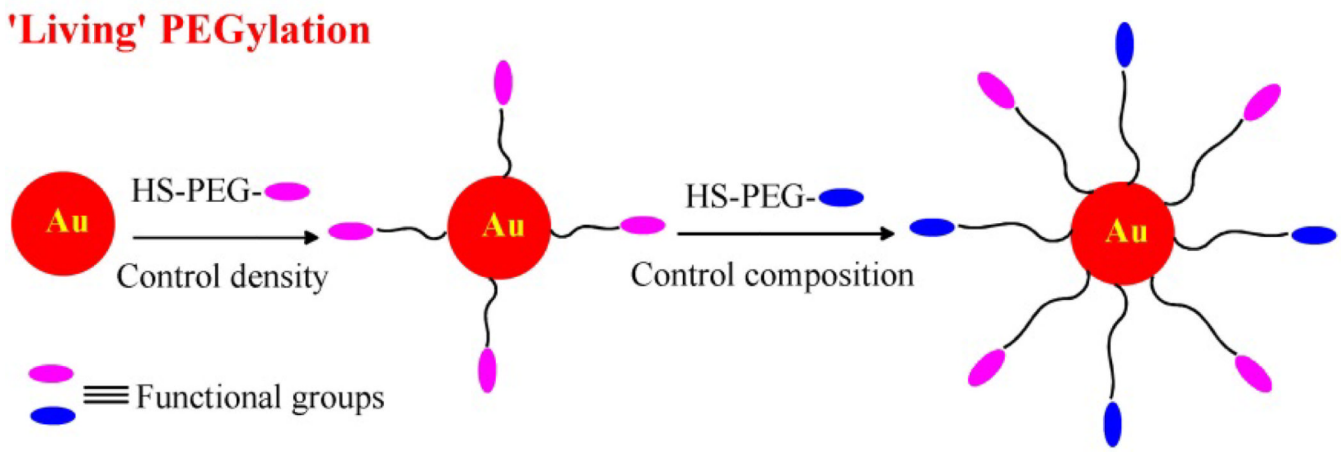

Scheme 1.
Schematic illustration of 'living' PEGylation with different functional PEG chains and controllable PEG chain density.